



Swansea University
Prifysgol Abertawe



Cronfa - Swansea University Open Access Repository

This is an author produced version of a paper published in:

Solar RRL

Cronfa URL for this paper:

<http://cronfa.swan.ac.uk/Record/cronfa51379>

Paper:

Kerremans, R., Sandberg, O., Meroni, S., Watson, T., Armin, A. & Meredith, P. (2019). On the ElectroOptics of Carbon Stack Perovskite Solar Cells. *Solar RRL*, 1900221

<http://dx.doi.org/10.1002/solr.201900221>

This item is brought to you by Swansea University. Any person downloading material is agreeing to abide by the terms of the repository licence. Copies of full text items may be used or reproduced in any format or medium, without prior permission for personal research or study, educational or non-commercial purposes only. The copyright for any work remains with the original author unless otherwise specified. The full-text must not be sold in any format or medium without the formal permission of the copyright holder.

Permission for multiple reproductions should be obtained from the original author.

Authors are personally responsible for adhering to copyright and publisher restrictions when uploading content to the repository.

<http://www.swansea.ac.uk/library/researchsupport/ris-support/>

On the Electro-Optics of Carbon Stack Perovskite Solar Cells

¹R. Kerremans, ¹O. J. Sandberg, ²S. Meroni, ²T. Watson, ^{1*}A. Armin & ^{1*}P. Meredith

¹ Department of Physics, Swansea University, Singleton Park, Swansea SA2 8PP United Kingdom

² SPECIFIC, College of Engineering, Swansea University Bay Campus, Swansea SA1 8EP United Kingdom

a.armin@swansea.ac.uk

paul.meredith@swansea.ac.uk

Abstract

The mesoporous carbon stack architecture is attracting considerable interest as a potential candidate for scalable, environmentally stable and low-cost perovskite solar cells amenable to high throughput manufacturing processes. These cells are characterised by microns-thick mesoporous titania and zirconia layers capped by a non-selective carbon top electrode with the whole stack being infused with a perovskite semiconductor. Although the architecture does not yet deliver the >20% power conversion efficiencies characteristic of some perovskite planar and mesoporous structures, it does appear to produce cells with respectable efficiencies >16% which is unexpected due to the carbon electrode being far from an ideal anode and the active layers being so thick. Full optimization of these cells requires a detailed understanding of the coupled efficiencies of light absorption, charge generation and extraction but the mode of operation is not yet understood. In this communication, we report a combined experimental-simulation study which elucidates the photogeneration and extraction of charge. By determination of the optical constants of the individual components of cell and using effective medium approximation, we determine the internal quantum efficiency (IQE) in both the titania and zirconia layers to be equally ~85%. Our numerical drift-diffusion simulations indicate that this high IQE together with a respectable open circuit voltage is a consequence of the thick junctions in play – reducing minority carrier concentrations at the electrodes and thereby decreasing surface recombination which is otherwise present in thinner cells with a non-selective contact. This insight can now be used to further tune the carbon stack for efficiency and simplicity.

Introduction

The organohalide perovskites are an intriguing class of semiconductors which can be processed from solution or evaporated at low temperatures from a range of simple, cheap and commonly available feedstocks. The modern manifestation of ‘perovskites’ originated quite recently from impressive performance as the semiconductor in thin film solar cells, but their applications have broadened to light emitting diodes (so called PLEDs now with external quantum efficiencies > 20% and rivalling mature organic LEDs)¹, photodetectors with detectivities close to silicon², and even rudimentary field effect transistors³. Perovskite solar cells have reached power conversion efficiencies (PCEs) of > 23%⁴ in a mesoporous scaffold architecture and > 21% in simple planar *nip* and *pin* structures⁵. It is thus no surprise that the race is on to commercialise perovskite photovoltaics both as stand-alone junctions⁶ and in tandems with silicon⁷.

There are many challenges to be overcome in ‘scaling’ a new optoelectronic technology to full product realisation. Thin film solar cells (for example based upon organic semiconductors) have proven particularly difficult to transition from the laboratory to the factory⁸ – and key stumbling blocks have (and continue to be) issues such as the relatively high sheet resistance of commercially available transparent conducting electrode materials, junction thickness inhomogeneities, long term stability⁹, and compatibility with suitable high throughput, low cost manufacturing processes. Perovskite solar cells face very similar scaling challenges, particularly the planar *nip* and *pin* structures where the junction thickness is < 500nm or so. An architecture recently proposed as a more scalable and manufacturable solution is the so-called mesoporous carbon stack. This cell design contains thick mesoporous zirconia and titania layers on the order of a micron, topped off with a mesoporous carbon electrode (anode) and infused with a perovskite semiconductor. The carbon anode is composed of nano-particulate graphene crystals conferring electrical conductance^{10,11}. In principle, all layers of this stack are printable, and indeed, various groups are now producing mini-modules with power conversion efficiencies of > 6% (aperture area of 198 cm²) using amino valeric acid-methyl ammonium lead iodide (AVA-MAPbI₃) as the perovskite semiconductor; see for example the work of Watson and co-workers¹²⁻¹⁵. The zirconia, titania and carbon layers of the modules of Watson et al. were screen printed from porous pastes and the MAPbI₃ ‘infused’ into the stack post deposition and annealing. The schematic of **Figure 1a** shows a typical carbon stack structure, a notable feature being the relatively thick carbon (~10 μm), zirconia (800 nm) and titania (1200 nm) layers. These form a considerably thicker ‘junction’ than other perovskite architectures and requires that photogenerated charges must traverse several microns to be extracted. Furthermore, there is the question of the work function of the carbon electrode being far from Ohmic and/or selective for holes. **Figure 1b** presents an energy level diagram of the carbon stack. Based on the energetics, it is clear that the carbon anode (with a work function of ~ 5eV¹⁰) can act as either a non-ideal anode or cathode. As such, while the dense crystalline titania (c-TiO₂) is an efficient, selective, electron extracting contact¹⁰, the carbon electrode is expected to be non-selective. Thus, an interesting general question arises as to whether perovskite cells in general require one or two selective contacts¹⁶ and more specifically as to how carbon stack perovskite solar cells operate at all.

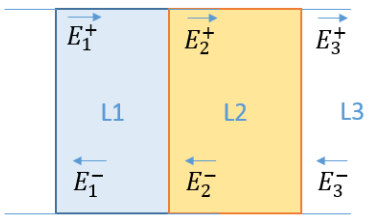
While some groups have already made good progress on the engineering problems of these cells¹⁷⁻¹⁹, the optimisation of the carbon stack cell has been a largely empirical exercise – questions of (for example) the optimal junction thickness have not been examined in any systematic manner and certainly not using the electro-optical simulation tools utilised in other perovskite architectures and organic semiconductor thin film solar cells²⁰. We have previously reported the use of transfer matrix field simulations coupled with ellipsometric and spectrophotometric analysis of thin film optical constants to predict the optimum junction and interlayer thicknesses in planar *nip*²¹ and *pin*²²

perovskite solar cells. The approach can also be used to accurately determine the internal quantum efficiency (IQE)^{20, 23} from the measured external quantum efficiency (EQE), and in the limit of low illumination intensities, the charge generation efficiency. The application of such an approach to the carbon stack is much more challenging because of the composite mesoporous nature of all layers, and the notorious difficulty in determining perovskite optical constants²⁴. Furthermore, the assumption of nearly perfect charge extraction in perovskite cells is no longer valid for carbon stack cells due to the large junction thickness and non-ideality of the work function of the carbon. This demands inclusion of full electro-optical device simulation using, for example, drift-diffusion methodologies. Understanding where, and with what efficiency, free carriers are generated and collected would allow rational improvements of the carbon stack device structure and the identification of voltage and current loss pathways.

Motivated by these questions we report a full electro-optical simulation of a previously empirically optimised carbon stack solar cell. We apply effective medium theory in combination with advanced ellipsometric and spectrophotometric measurements to accurately determine the composite optical constants of the mesoporous layers and are thus able to simulate the absorbed photon profiles in the junction layers. From this, and by comparing with the measured EQE, we evaluate the internal quantum efficiency for charge collection in both the zirconia and titania elements of the junction. Feeding the charge generation profiles into our drift-diffusion model we are also able to numerically quantify charge carrier recombination in these cells and explain their mode of operation. We find that the carbon stack cells with non-ideal anodes only work because they are very thick. The large optical density of these devices reduces the amount of electrons generated near the carbon anode reducing the overall surface recombination rate even though the surface recombination velocity is expected to be large due to the non-selectivity of the carbon electrode.

Experimental

The Transfer Matrix Method: The Abeles transfer matrix method allows one to compute the optical field distribution in any multilayer stack^{25, 26}. The only requirement for this method is accurate knowledge of layer thicknesses and refractive indices, which can be determined experimentally with a combination of single-layer ellipsometry, profilometry, and spectrophotometry^{27, 28}. The fundamentals of the methodology are well known²⁹ but amount to the definition of a propagation matrix for each of the layers in an arbitrary stack as follows:

$$\begin{pmatrix} E_1^+ \\ E_1^- \end{pmatrix} = \frac{1}{t_{12}} \begin{pmatrix} \varphi_1^{-1} & 0 \\ 0 & \varphi_1 \end{pmatrix} \begin{pmatrix} 1 & r_{12} \\ r_{21} & 1 \end{pmatrix} \begin{pmatrix} E_2^+ \\ E_2^- \end{pmatrix} + \frac{1}{t_{23}} \begin{pmatrix} \varphi_2^{-1} & 0 \\ 0 & \varphi_2 \end{pmatrix} \begin{pmatrix} 1 & r_{23} \\ r_{32} & 1 \end{pmatrix} \begin{pmatrix} E_3^+ \\ E_3^- \end{pmatrix}$$


where r_{ij} and t_{ij} are the Fresnel coefficients and $\varphi_L = \exp(i 2\pi n_L t_L / \lambda)$ is the phase operator for each layer, dependent on the wavelength, thickness and complex refractive index, $\underline{n}_L = n + ik$. Each layer effectively adds another matrix to the transfer matrix product, which lets us determine the forwards-and-backwards-propagating optical electric field E_i at each layer interface. Thus, the optical field throughout the stack can be modelled if the layer constants are known. From this field distribution, we can then derive the charge photogeneration distribution in the active layers, which can in turn be used to determine the ideal device EQE, under global AM1.5 radiation or any other illumination.

Optical Constant Determination: A combination of spectroscopic ellipsometry (JA Woollam M2000) and reflection and transmission spectrophotometry (Perkin Elmer λ 950 equipped with universal reflectance attachment and 150 mm integrating sphere) were used to accurately determine the optical constants of each of the constituents of the carbon stack. Samples for this analysis were prepared as single layers on glass (the experimental conditions for the deposition of each layer are provided in the Supplementary Information) with thicknesses relevant to the full cell structure (from the fluorine doped tin oxide (FTO): 600, 50, 800, 1200, and 3000 nm respectively; see **Figure 1a**). The dense titania was modelled as a single homogeneous layer, and the graded FTO was implemented in the ellipsometric model as separate layers of 'SnO₂' and 'SnOF' (regular and fluorinated tin oxide), with thicknesses of 100 and 500 nm respectively. This treatment of FTO as two separate layers is justified by a spectrophotometric analysis (reflectance and transmittance measurement and simulations) as shown in the **Supplementary Information (Figure S2)**. Constant determination of the mesoporous titania, zirconia and MAPI₃ is considerably more complicated than either the FTO or dense TiO₂ – the mesoporous oxide layers are inhomogeneous and scattering, and the perovskite is polycrystalline with high dispersion in both n and k . We have previously published a methodology and the resultant optical constants for MAPI₃²⁷, which we utilise in this current study since they have been verified by experimental measurement of short circuit current density and EQE. As indicated previously, the mesoporous titania and zirconia cannot be thought of as compositionally homogeneous, and their optical constants scale with pore volume fraction in a manner predicted by the effective medium approximation³⁰. To determine the pore volume in both materials, ellipsometric porosimetry with dynamic toluene infiltration was utilised (see **Supplementary Information**), the results of which are shown in **Figure 2(a)**. The pore volume fraction was determined to be approximately 0.5 in both cases. This value was then used to determine the relative optical constants of the mesoporous titania and zirconia layers with and without perovskite infiltration using the Bruggeman Effective Medium approximation:

$$f_a \frac{\epsilon_a - \epsilon}{\epsilon_a + 2\epsilon} + (1 - f_a) \frac{\epsilon_b - \epsilon}{\epsilon_b + 2\epsilon} = 0 \quad (1)$$

where f_a and $(1-f_a)$ represent the probabilities of finding the respective materials of dielectric constants ϵ_a and ϵ_b in a spherical space and can be interpreted as a volume ratio. All optical constants for the FTO, dense titania and mesoporous zirconia and titania are provided in **Figure S1** in the **Supplementary Information**. The mesoporous titania and zirconia infiltrated with MAPI₃ assuming 100% pore filling are shown in **Figure 2b**. These data enable a full modelling of the optical field distribution in the entire carbon stack solar cell.

Carbon Stack Multilayer Model & Quantum Efficiency (External & Internal): The stack model was implemented in Matlab using a standard Transfer Matrix approach with layers: 'Air', 'Glass', 'FTO', 'compact TiO₂', 'mesoporous TiO_x', 'mesoporous ZrO_x', and 'mesoporous Carbon' (**Figure 3**), where the glass was treated as incoherent (i.e. optically thick relative to the wavelength of incident light). The modelled thicknesses of the optically coherent layers, starting with the FTO in nm, were again 600, 50, 800, 1200, and 3000 as per the estimated experimental thicknesses of the empirically optimised cell structures.

The experimentally measured External Quantum Efficiency ($EQE_{exp}(\lambda)$) can be considered as the sum of the EQEs of the two absorbing components titania-MAPI₃ and zirconia-MAPI₃. This in turn can be considered as the sum of the optical absorbance $A(\lambda)$ in each component scaled by the Internal Quantum Efficiency (IQE) such that:

$$EQE_{exp}(\lambda) = IQE_{TiO_2} \cdot A_{TiO_2}(\lambda) + IQE_{ZrO_2} \cdot A_{ZrO_2}(\lambda) \quad (2)$$

The Internal Quantum Efficiency of solar cells with MAPi_3 as the active component (or indeed other high efficiency perovskite systems) has been shown to be spectrally invariant²⁷. Hence by comparing the experimentally measured and simulated absorbances from the Transfer Matrix analysis (which is equivalent to the EQE assuming 100% generation and collection efficiency) the individual IQEs can be extracted.

Results and Discussion

Figure 3 shows the calculated charge generation spatial profile ($G(z)$) for two wavelengths, one which should be strongly absorbed by the titania- MAPi_3 (400 nm) and one in the tail of the perovskite absorption. Notably, and as expected intuitively, carriers derived from blue photons are generated with a Beer-Lambert profile within the first 500 nm of the titania- MAPi_3 layer. Conversely, those generated from red photon absorption extend throughout both layers to the top carbon contact and show the typical modulations indicative of low-Q cavity interference. Simulations at every wavelength from 400 nm to 800 nm allow a full reconstruction of the EQE which is shown in **Figure 4a** overlaid on a typical experimentally measured EQE. There is a clear discrepancy between the simulated and experimental spectra although they have the same shape as a function of wavelength – this difference being due to the real non-unity of the IQEs in the two charge generating layers due to both geminate and non-geminate recombination losses.

Equation 2 can now be used to extract $\text{IQE}_{\text{TiO}_2}$ and $\text{IQE}_{\text{ZrO}_2}$ by a two-parameter global fit, once again noting the spectral flatness of the IQEs. **Figure 4b** shows the best fit for this analysis from which the parameters are extracted. It should be noted that the fitting range was truncated at 760 nm where the experimental EQE decreases precipitously near the MAPi_3 band edge and hence the fitting error diverges rapidly (see **Figure S3**). From this analysis we extract internal quantum efficiencies of 0.87 and 0.86 for the titania- MAPi_3 and zirconia- MAPi_3 layers respectively, i.e. implying that the efficiency with which photogenerated charge is extracted is very similar in the two cases. We also determined the numerical fitting sensitivity for these values based upon an error sensitivity analysis of the fitting procedure (**Supplementary Figure S4**).

These are interesting findings for two key reasons:

- i) the relatively high IQEs mean that holes generated in the titania- MAPi_3 can be efficiently transported several microns (including through the zirconia- MAPi_3) to be extracted at the carbon anode, and likewise electrons generated in the zirconia- MAPi_3 layer to be extracted at the FTO cathode;
- ii) electrons and holes are transported with similar efficiencies through the two layers even though zirconia is a wide gap insulator and titania an n-type semiconductor – i.e. they have very different electrical properties.

One could therefore surmise that the infused MAPi_3 plays a dominant role in transporting photogenerated charge carriers over relatively large distances with recombination loss mainly at the interfaces. Free carrier diffusion lengths in various perovskites have been estimated to be up to several hundred microns³¹, and so maybe this should not come as too great a surprise in these carbon stack cells. Clearly, the non-selectivity of the carbon (nanocrystalline graphene) anode does not suppress hole collection at short-circuit and we turn to this question later in the communication.

In addition, a direct application of our optical model is to predict the optimal thickness of the optically active layers to achieve maximum short-circuit current density (J_{SC}). **Figure 5a** shows the predicted short-circuit current density as a function of the active layer thickness d , assuming an IQE of 100%, for a fixed thickness ratio of 2/3 between the m-TiOx and m-ZrOx (see **Figure 1a**). It can be seen that,

while a thickness $d > 1 \mu\text{m}$ is needed to avoid substantial losses in absorption, increasing the active layer beyond $d = 2.5 \mu\text{m}$ increases the maximal J_{SC} only marginally. We note that interference effects, generally expected at the lower active layer thicknesses, are small in these types of structures because of the poorly reflecting mesoporous carbon (back) contact.

Whilst the J_{SC} is expected to be relatively unaffected by the non-selectivity of the carbon electrode due to the reduced carrier concentration under short circuit conditions, it is well-known that the open-circuit voltage (V_{OC}) is highly susceptible to non-selective contacts with non-optimized energy levels, in particular in systems exhibiting relatively high carrier mobilities where the carrier diffusion is considered long range^{32,33}. In this regard it is likely that the carbon work function mismatch with the MAPbI_3 valence band edge produces a Schottky rather than a perfectly Ohmic contact. To clarify the role of the non-selective carbon anode, we combine the optical model with electrical device simulations based on a numerical drift-diffusion model^{33,34}. **Figure 5b** shows the qualitative thickness dependence of the open-circuit voltage, for the system depicted in **Figure 1b**, treating the carbon as a non-selective electrode with respect to the extraction of electrons and holes. The optically active layer is treated as an effective medium with an electron and hole mobility of $10 \text{ cm}^2\text{V}^{-1}\text{s}^{-1}$, whereas the FTO/c-TiO₂ layer is assumed an electron-selective cathode. For comparison, we have also included the idealized case of a selective, hole-only extracting anode. The corresponding effect of the selectivity of the anode and the thickness of the optically active layer on current-voltage characteristics is simulated in **Figure 5c** and **Figure 5d**.

In the simulations (**Figure 5**), a hole-selective contact is realized by setting the electron current to be zero at the anode contact. For the non-selective case, the contact instead acts as a sink for both electrons and holes: this is realized by requiring that the electron density at the contact maintains its equilibrium value during solar cell operating conditions, so that the electron density at the anode contact is given by $N_c \exp(-\phi_{Bn}/kT)$. Here, ϕ_{Bn} is the Schottky barrier height for electrons at the anode contact (the difference between the conduction band edge of the active layer and the Fermi level of the anode), whereas N_c is the effective density of states for electrons in the active layer. Furthermore, we assume a dielectric constant of 13, effective density of states of 10^{19} cm^{-3} , and second-order recombination with a coefficient of $6 \times 10^{-11} \text{ cm}^3/\text{s}$. The corresponding carrier density profiles for the devices in **Figure 5(c)** and **(d)** under short-circuit and open-circuit conditions have been simulated in **Figure 6**.

Based on these simulations, it can be concluded that the main loss induced by the non-selectivity of the carbon electrode manifests as a loss in the open-circuit voltage. The loss in photovoltage is a direct consequence of the large surface recombination caused by unintentional extraction of electrons at the carbon contact. While this loss can be reduced in principle by making the carbon electrode selective for the extraction of holes, this strategy might be non-trivial in practice, though attempts have already been made³⁵. However, the surface recombination loss can also be reduced by making the active layer thicker. This is to be expected considering that most of the charge carriers are generated close to the c-TiO₂ contact; by increasing the active layer thickness the number of electrons generated near the carbon contact can be reduced thus also reducing the unintentional extraction of electrons at this contact. Owing to the electron-selectivity of the c-TiO₂ layer, holes in turn will drift-diffuse towards the carbon contact, without substantial recombination in the bulk (be it first or second order). We note, however, that the surface recombination loss of electrons at the non-selective contact is also highly sensitive to the electron mobility.

It should also be pointed out that the fill factor is strongly dependent on the prevailing charge transport and recombination parameters, as well as external resistive effects, and is therefore in general also influenced by the thickness of the optically active layer. Further experiments such as

injection-CELIV³⁶, or intensity-dependent photocurrent measurements³⁷, would allow us to probe the recombination mechanisms at play. This in turn would facilitate more accurate electro-optical device simulations, allowing us to make genuine layer thickness optimizations that account for most parameters as per conventional, planar cells³⁸⁻⁴⁰. This work is underway.

Conclusions

The carbon stack architecture is widely viewed as a possible candidate for low cost, manufacturable perovskite solar cells. We have developed an optical model based upon composite mesoporous oxide-perovskite absorbing, charge generating layers (titania-MAPbI₃ and zirconia-MAPbI₃) and using a Transfer Matrix approach simulated the External Quantum Efficiency of a previously empirically optimised operational device. Comparison of these simulations with the experimental EQEs has allowed us to estimate the Internal Quantum Efficiency (charge generation and extraction) to be of order 0.85 in both composite layers. This is a somewhat surprising result given the transport distances involved and the poor electrical properties of the zirconia in particular. We therefore conclude that the infused MAPbI₃ plays a significant role in the transport of electrons to the FTO cathode and holes to the carbon anode. Furthermore, we find that a thick junction is essential to reduce surface recombination (i.e. unintentional extraction) of electrons at the non-selective carbon contact. This unintentional extraction of electrons at the anode results in large open-circuit voltage losses in thinner junctions.

Acknowledgements

This work was funded by the Welsh Government's Sêr Cymru II Program (Sustainable Advanced Materials) through the European Regional Development Fund and Welsh European Funding Office. R.K. is the recipient of an EPSRC DTP postgraduate award. P.M. is a Sêr Cymru II Research Chair and A.A. a Sêr Cymru II Rising Star Fellow. We acknowledge the assistance of J. Van Derslice at J.A. Woollam for assistance with the porosimetry measurements. This work was also supported by the Engineering and Physical Sciences Research Council (EPSRC) through the 'Self Assembling Perovskite Absorbers – Cells Engineered into Modules' project (EP/M015254/1) and the SPECIFIC Innovation and Knowledge Centre (EP/N020863/1). This work was also partially funded by the Institutional Links grant, ID 332397170, under the Newton Fund partnership. The grant is funded by the UK Department for Business, Energy and Industrial Strategy and SENER-CONACyT and delivered by the British Council.

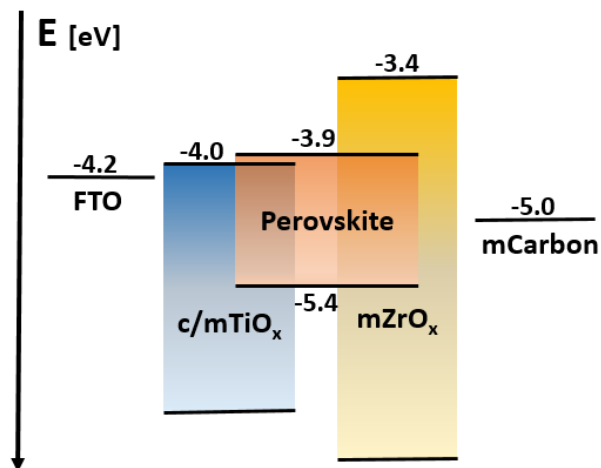
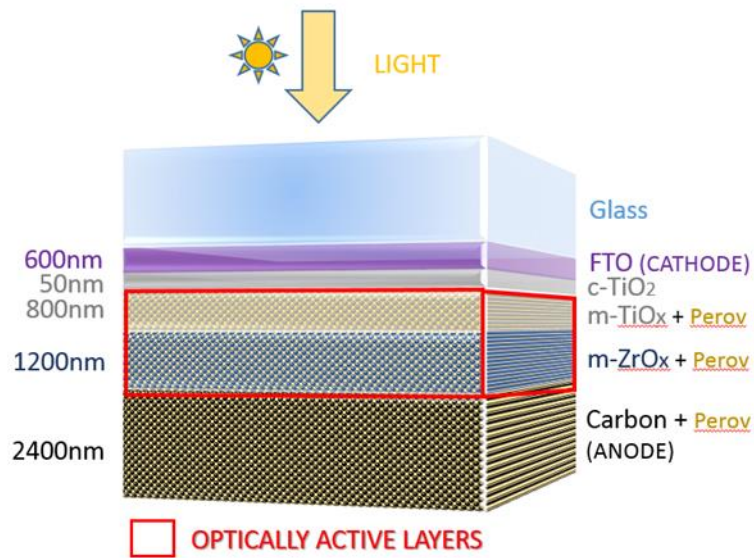


Figure 1. The carbon stack perovskite solar cell: **(a)** A multilayer schematic representation of the carbon stack perovskite solar cell built upon a glass-FTO (fluorine doped tin oxide - cathode) substrate with subsequent layers of dense, crystalline titania (c-TiO₂), mesoporous titania and MAPI₃ (perov), mesoporous zirconia and MAPI₃ (perov), and carbon (nanocrystalline graphene) anode. The optically active layers are boxed in red. **(b)** An approximate flat band energy level diagram for this structure with values extracted from known literature or measured by Kelvin Probe Microscopy or Ultraviolet Photoemission Spectroscopy.

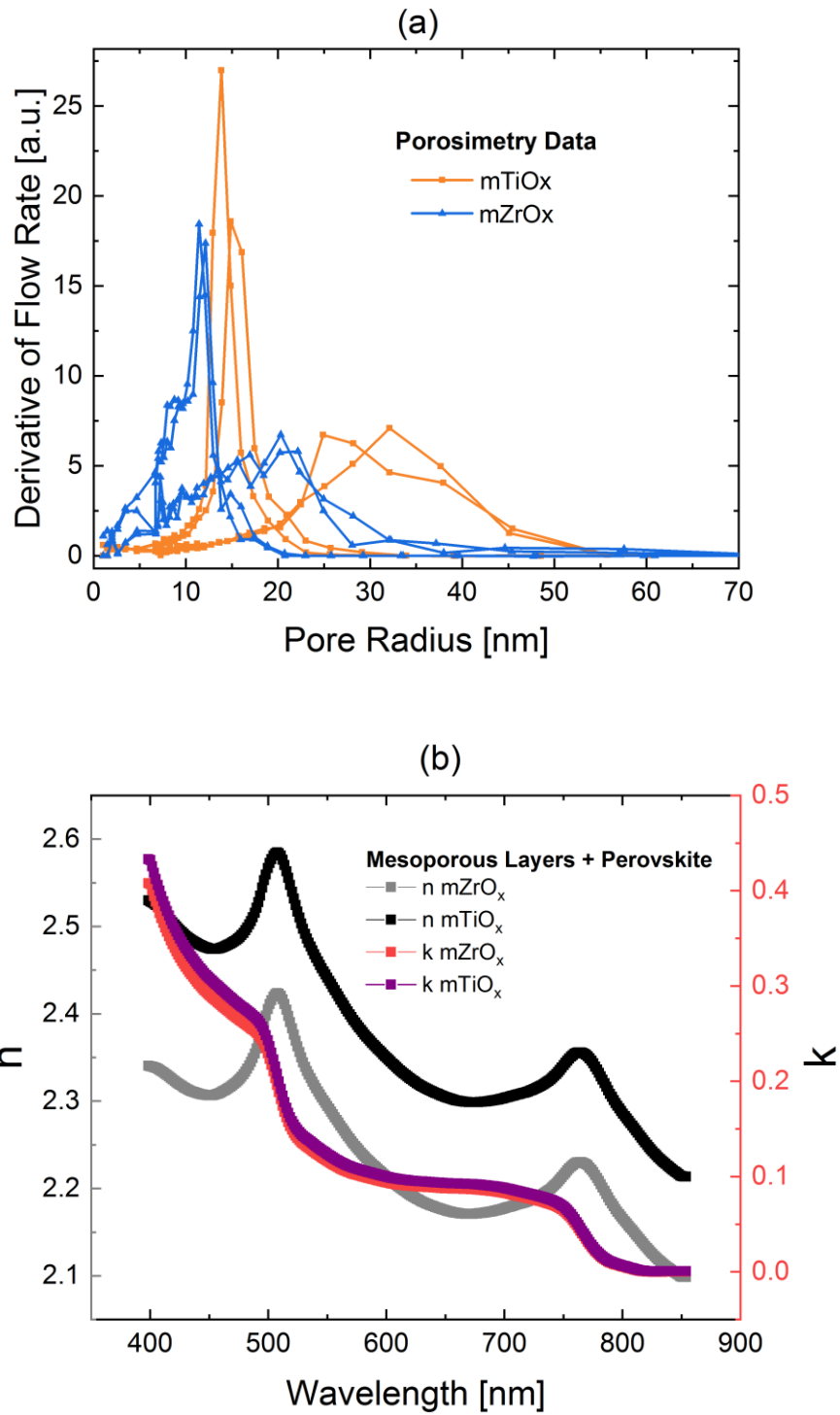


Figure 2. Mesoporous oxide-perovskite composite layer optical constants: **(a)** Results of porosimetry obtained with dynamic ellipsometry with toluene infiltration of the two mesoporous layers. Both active materials (m-TiO_x and m-ZrO_x) have a pore radius on the scale of 10-20nm and can be shown to have volume fractions of respectively 51 and 49%. **(b)** Optical constants (refractive index and extinction coefficients) of the two active layers after MAPI₃ infiltration, using the Bruggeman effective index model. The model assumes full infiltration as well as previously derived MAPI₃ optical constants²⁷.

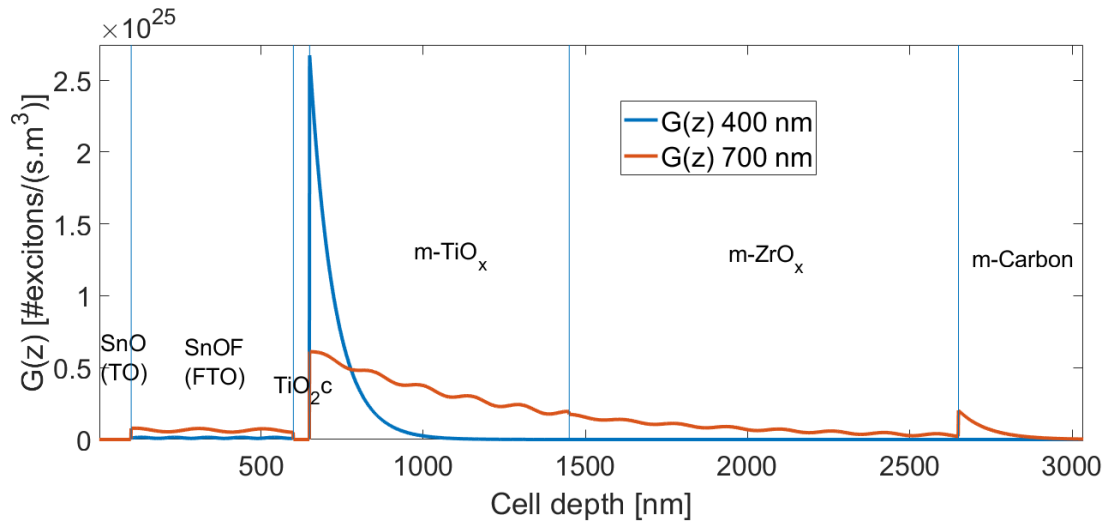


Figure 3. Spatial profile of photo-generated charges in the multilayer carbon stack solar cell at 400nm and 700nm incident light wavelengths (as examples). The generation profile is determined from a Transfer Matrix simulation of the optical field distribution assuming unity Internal Quantum Efficiency. Light is incident from left and propagates to the right.

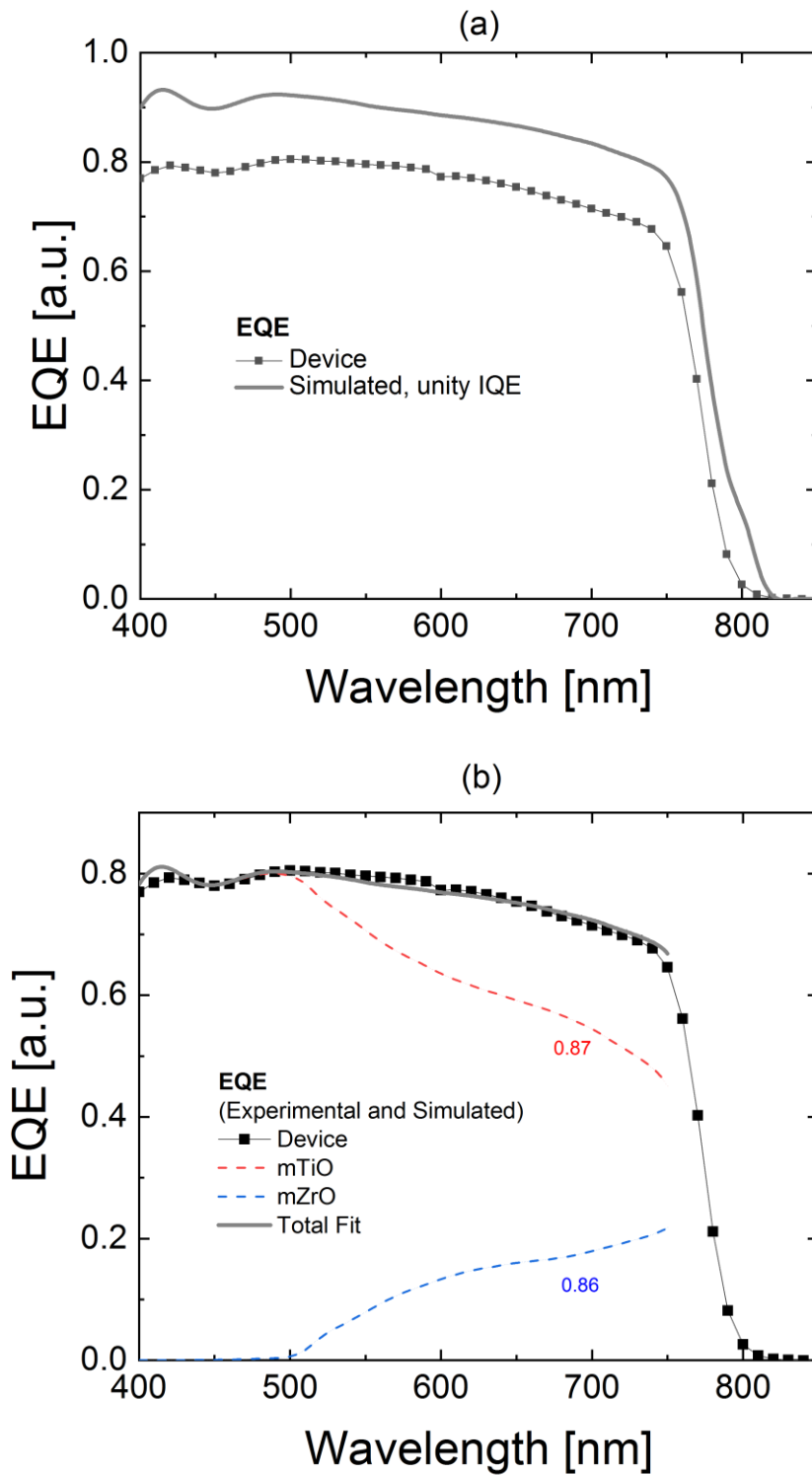


Figure 4. External Quantum Efficiencies (EQE) – experimental values compared with simulations for the case of (a) unity Internal Quantum Efficiency (IQE), and (b) non-unity, spectrally flat IQEs determined from a two-parameter fit (**Supplementary Information Figure S5**). The analysis yields IQE's of 0.87 and 0.86 in the titania and zirconia layers respectively.

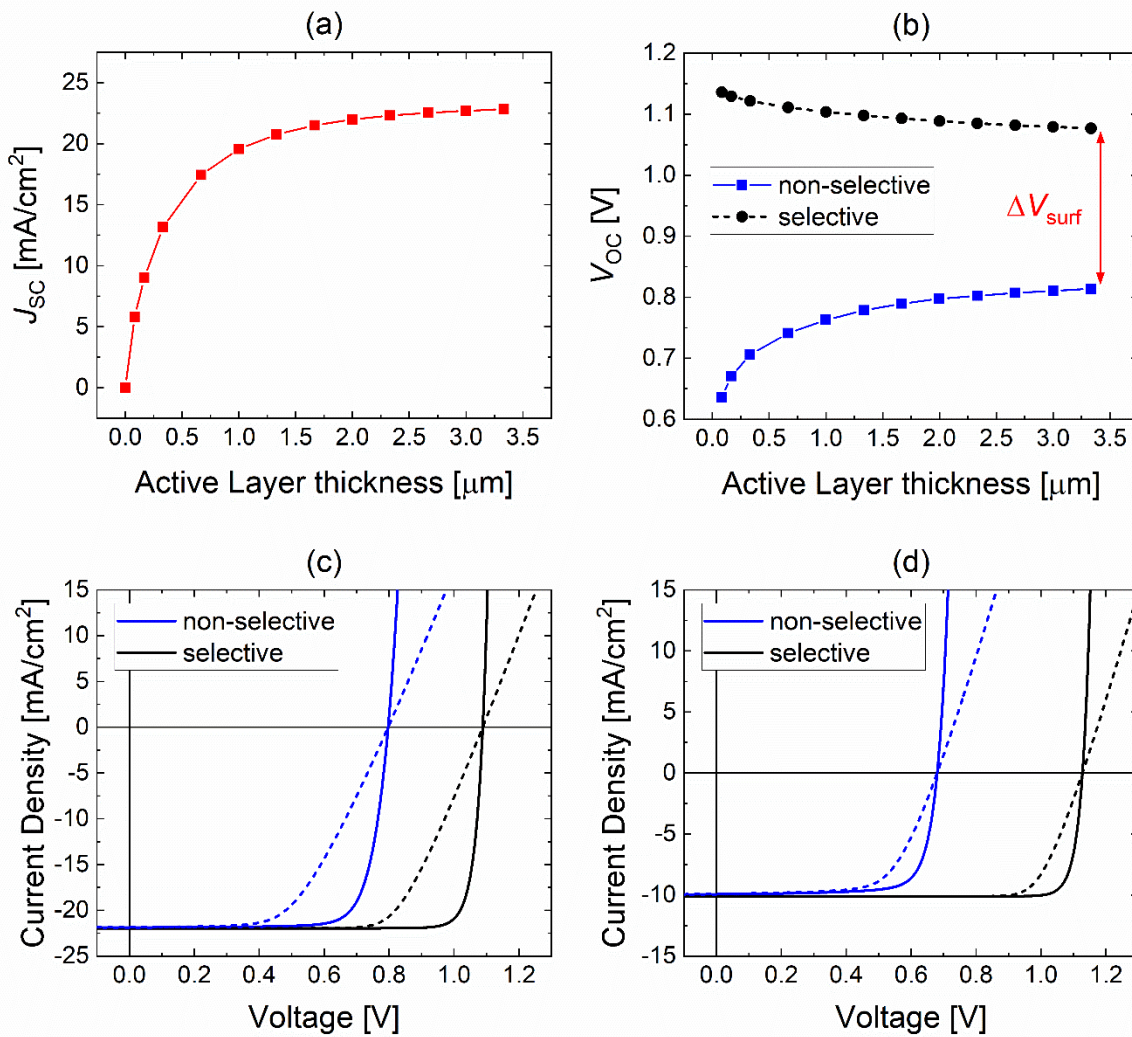


Figure 5. Simulated thickness dependence: (a) shows the short-circuit current density vs. active layer thickness as predicted by the optical model, assuming an IQE of 100%; (b) shows the corresponding qualitative active layer thickness dependence of the open-circuit voltage, as obtained by electrical device simulations, for the case with a selective and a non-selective carbon contact. A thickness ratio of 2/3 between m-TiOx and m-ZrOx layers (see **Figure 1a**) within the optically active layer is assumed. The simulated current-voltage characteristics under 1 sun incident illumination are shown at an active layer thickness of (c) 2000 nm and (d) 200 nm. The solid and dashed lines correspond to the cases with an external series resistance (from the electrodes and the external wires) of 0 and 10 Ωcm^2 , respectively.

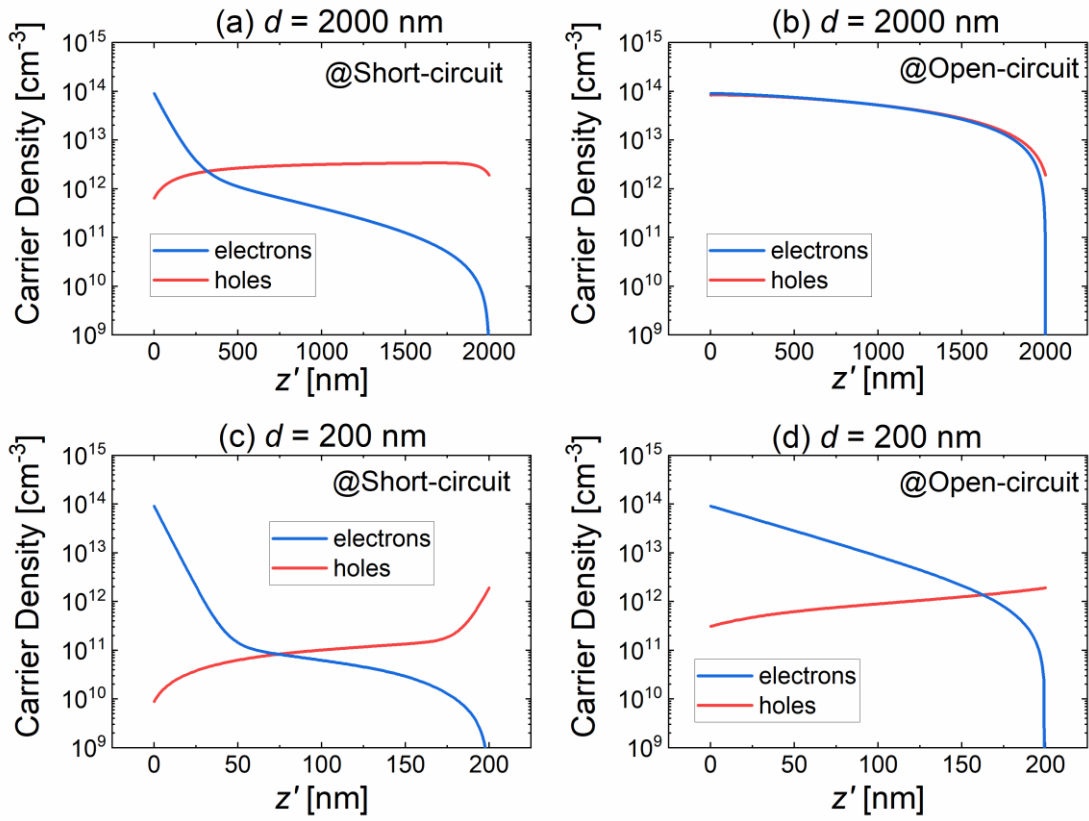


Figure 6. The charge carrier distributions inside the active layer under 1 sun incident illumination using the combined optical and electrical device model simulated at short-circuit and open-circuit for the case with a non-selective carbon electrode. Here, the c-TiO₂ contact is at $z' = 0$, whereas the non-selective carbon contact is at $z' = d$. In all of the electrical device simulations, an energy level structure defined by **Figure 1b** is assumed. Furthermore, electron and hole mobilities of 10 cm²/Vs, a dielectric constant of 13, effective density of states of 10¹⁹ cm⁻³, and second-order recombination with a coefficient of 6×10^{-11} cm³/s are assumed.

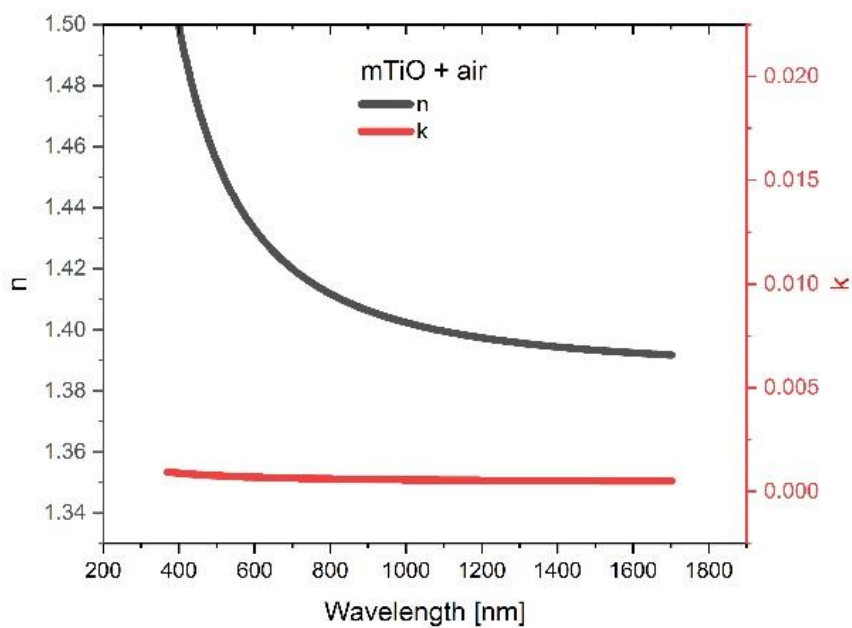
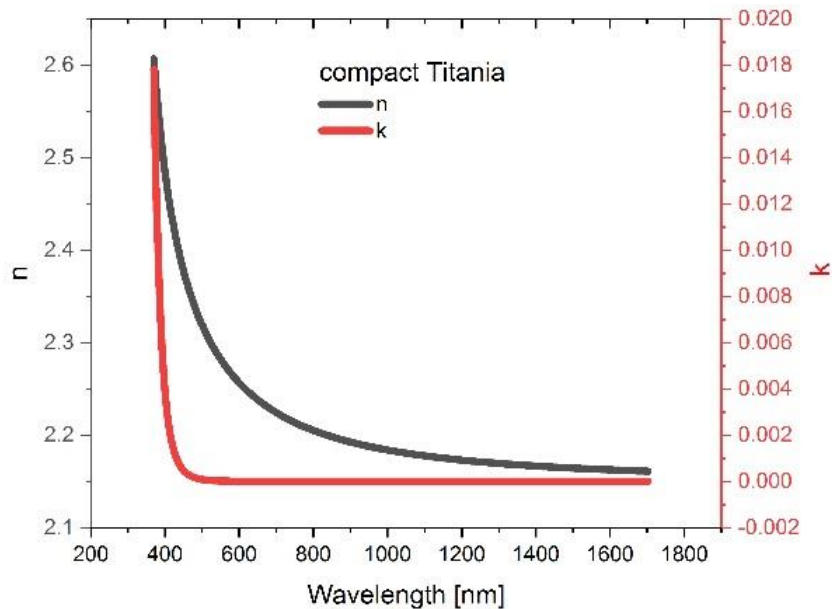
References

1. Meredith P, Armin A. LED technology breaks performance barrier. 2018.
2. Tan Z, Wu Y, Hong H, Yin J, Zhang J, Lin L, Wang M, Sun X, Sun L, Huang Y. Two-dimensional (C₄H₉NH₃)₂PbBr₄ perovskite crystals for high-performance photodetector. *Journal of the American Chemical Society* 2016, 138:16612-16615.
3. Chin XY, Cortecchia D, Yin J, Bruno A, Soci C. Lead iodide perovskite light-emitting field-effect transistor. *Nature communications* 2015, 6:7383.
4. Jeon NJ, Na H, Jung EH, Yang T-Y, Lee YG, Kim G, Shin H-W, Seok SI, Lee J, Seo J. A fluorene-terminated hole-transporting material for highly efficient and stable perovskite solar cells. *Nature Energy* 2018, 3:682.
5. Saliba M, Correa-Baena J-P, Wolff CM, Stolterfoht M, Phung N, Albrecht S, Neher D, Abate A. How to make over 20% efficient perovskite solar cells in regular (n-i-p) and inverted (p-i-n) architectures. *Chemistry of Materials* 2018, 30:4193-4201.
6. Rong Y, Hu Y, Mei A, Tan H, Saidaminov MI, Seok SI, McGehee MD, Sargent EH, Han H. Challenges for commercializing perovskite solar cells. *Science* 2018, 361:eaat8235.
7. Sahli F, Werner J, Kamino BA, Bräuning M, Monnard R, Paviet-Salomon B, Barraud L, Ding L, Leon JJD, Sacchetto D. Fully textured monolithic perovskite/silicon tandem solar cells with 25.2% power conversion efficiency. *Nature materials* 2018, 17:820.
8. Meng L, You J, Yang Y. Addressing the stability issue of perovskite solar cells for commercial applications. *Nature communications* 2018, 9:5265.
9. Grancini G, Roldán-Carmona C, Zimmermann I, Mosconi E, Lee X, Martineau D, Narbey S, Oswald F, De Angelis F, Graetzel M. One-Year stable perovskite solar cells by 2D/3D interface engineering. *Nature communications* 2017, 8:15684.
10. Mei A, Li X, Liu L, Ku Z, Liu T, Rong Y, Xu M, Hu M, Chen J, Yang Y. A hole-conductor-free, fully printable mesoscopic perovskite solar cell with high stability. *Science* 2014, 345:295-298.
11. Shao L-L, Chen M, Ren T-Z, Yuan Z-Y. Ordered mesoporous carbon/graphene nano-sheets composites as counter electrodes in dye-sensitized solar cells. *Journal of power sources* 2015, 274:791-798.
12. De Rossi F, Baker JA, Beynon D, Hooper KE, Meroni SM, Williams D, Wei Z, Yasin A, Charbonneau C, Jewell EH. All printable perovskite solar modules with 198 cm² active area and over 6% efficiency. *Advanced Materials Technologies* 2018, 3:1800156.
13. Meroni SM, Mouhamad Y, De Rossi F, Pockett A, Baker J, Escalante R, Searle J, Carnie MJ, Jewell E, Oskam G. Homogeneous and highly controlled deposition of low viscosity inks and application on fully printable perovskite solar cells. *Science and Technology of Advanced Materials* 2018, 19:1-9.
14. Lee HKH, Barbé J, Meroni SM, Du T, Lin CT, Pockett A, Troughton J, Jain SM, De Rossi F, Baker J. Outstanding Indoor Performance of Perovskite Photovoltaic Cells—Effect of Device Architectures and Interlayers. *Solar RRL* 2019, 3:1800207.
15. Baker J, Hooper K, Meroni S, Pockett A, McGettrick J, Wei Z, Escalante R, Oskam G, Carnie M, Watson T. High throughput fabrication of mesoporous carbon perovskite solar cells. *Journal of Materials Chemistry A* 2017, 5:18643-18650.
16. Juarez-Perez EJ, Wußler M, Fabregat-Santiago F, Lakus-Wollny K, Mankel E, Mayer T, Jaegermann W, Mora-Sero I. Role of the selective contacts in the performance of lead halide perovskite solar cells. *The journal of physical chemistry letters* 2014, 5:680-685.
17. Meng F, Liu A, Gao L, Cao J, Yan Y, Wang N, Fan M, Wei G, Ma T. Current Progress in Interfacial Engineering of Carbon-Based Perovskite Solar Cells. *Journal of Materials Chemistry A* 2019.
18. Zimmermann I, Gratia P, Martineau D, Grancini G, Audinot JN, Wirtz T, Nazeeruddin MK. Improved efficiency and reduced hysteresis in ultra-stable fully-printable mesoscopic perovskite solar cells through incorporation of CuSCN in the perovskite layer. *Journal of Materials Chemistry A* 2019.

19. Mishra A, Ahmad Z, Zimmermann I, Martineau D, Shakoor R, Touati F, Riaz K, Al-Muhtaseb SA, Nazeeruddin MK. Effect of annealing temperature on the performance of printable carbon electrodes for perovskite solar cells. *Organic Electronics* 2019, 65:375-380.
20. Armin A, Velusamy M, Wolfer P, Zhang Y, Burn PL, Meredith P, Pivrikas A. Quantum Efficiency of Organic Solar Cells: Electro-Optical Cavity Considerations. *ACS Photonics* 2014, 1:173-181.
21. Huang Y-C, Tsao C-S, Cho Y-J, Chen K-C, Chiang K-M, Hsiao S-Y, Chen C-W, Su C-J, Jeng U-S, Lin H-W. Insight into evolution, processing and performance of multi-length-scale structures in planar heterojunction perovskite solar cells. *Scientific reports* 2015, 5:13657.
22. Zhang S, Stolterfoht M, Armin A, Lin Q, Zu F, Sobus J, Jin H, Koch N, Meredith P, Burn PL. Interface Engineering of Solution-Processed Hybrid Organohalide Perovskite Solar Cells. *ACS applied materials & interfaces* 2018, 10:21681-21687.
23. Armin A, Zhang Y, Burn PL, Meredith P, Pivrikas A. Measuring internal quantum efficiency to demonstrate hot exciton dissociation. *Nature materials* 2013, 12:593.
24. Pettersson LA, Roman LS, Inganäs O. Quantum efficiency of exciton-to-charge generation in organic photovoltaic devices. *Journal of Applied Physics* 2001, 89:5564-5569.
25. Pettersson LA, Roman LS, Inganäs O. Modeling photocurrent action spectra of photovoltaic devices based on organic thin films. *Journal of Applied Physics* 1999, 86:487-496.
26. Ohta K, Ishida H. Matrix formalism for calculation of electric field intensity of light in stratified multilayered films. *Applied optics* 1990, 29:1952-1959.
27. Lin Q, Armin A, Nagiri RCR, Burn PL, Meredith P. Electro-optics of perovskite solar cells. *Nature Photonics* 2015, 9:106.
28. Mahamuda S, Swapna K, Rao AS, Jayasimhadri M, Sasikala T, Pavani K, Moorthy LR. Spectroscopic properties and luminescence behavior of Nd³⁺ doped zinc alumino bismuth borate glasses. *Journal of Physics and Chemistry of Solids* 2013, 74:1308-1315.
29. Heavens OS. *Optical properties of thin solid films*: Courier Corporation; 1991.
30. Aspnes D. Local-field effects and effective-medium theory: a microscopic perspective. *American Journal of Physics* 1982, 50:704-709.
31. Wehrenfennig C, Eperon GE, Johnston MB, Snaith HJ, Herz LM. High charge carrier mobilities and lifetimes in organolead trihalide perovskites. *Advanced materials* 2014, 26:1584-1589.
32. Tress W, Leo K, Riede M. Optimum mobility, contact properties, and open-circuit voltage of organic solar cells: A drift-diffusion simulation study. *Physical Review B* 2012, 85:155201.
33. Sandberg OJ, Sundqvist A, Nyman M, Österbacka R. Relating charge transport, contact properties, and recombination to open-circuit voltage in sandwich-type thin-film solar cells. *Physical Review Applied* 2016, 5:044005.
34. Sherkar TS, Momblona C, Gil-Escrig L, Bolink HJ, Koster LJA. Improving perovskite solar cells: Insights from a validated device model. *Advanced Energy Materials* 2017, 7:1602432.
35. Cao K, Zuo Z, Cui J, Shen Y, Moehl T, Zakeeruddin SM, Grätzel M, Wang M. Efficient screen printed perovskite solar cells based on mesoscopic TiO₂/Al₂O₃/NiO/carbon architecture. *Nano Energy* 2015, 17:171-179.
36. Armin A, Juska G, Ullah M, Velusamy M, Burn PL, Meredith P, Pivrikas A. Balanced Carrier Mobilities: Not a Necessary Condition for High-Efficiency Thin Organic Solar Cells as Determined by MIS-CELIV. *Advanced Energy Materials* 2014, 4:1300954.
37. Stolterfoht M, Armin A, Shoaee S, Kassal I, Burn P, Meredith P. Slower carriers limit charge generation in organic semiconductor light-harvesting systems. *Nature communications* 2016, 7:11944.
38. Barker JA, Ramsdale CM, Greenham NC. Modeling the current-voltage characteristics of bilayer polymer photovoltaic devices. *Physical Review B* 2003, 67:075205.
39. Inche Ibrahim ML, Ahmad Z, Sulaiman K. Analytical expression for the current-voltage characteristics of organic bulk heterojunction solar cells. *AIP Advances* 2015, 5:027115.

40. Häusermann R, Knapp E, Moos M, Reinke NA, Flatz T, Ruhstaller B. Coupled optoelectronic simulation of organic bulk-heterojunction solar cells: Parameter extraction and sensitivity analysis. *Journal of Applied Physics* 2009, 106:104507.

SUPPLEMENTARY INFORMATION FIGURES



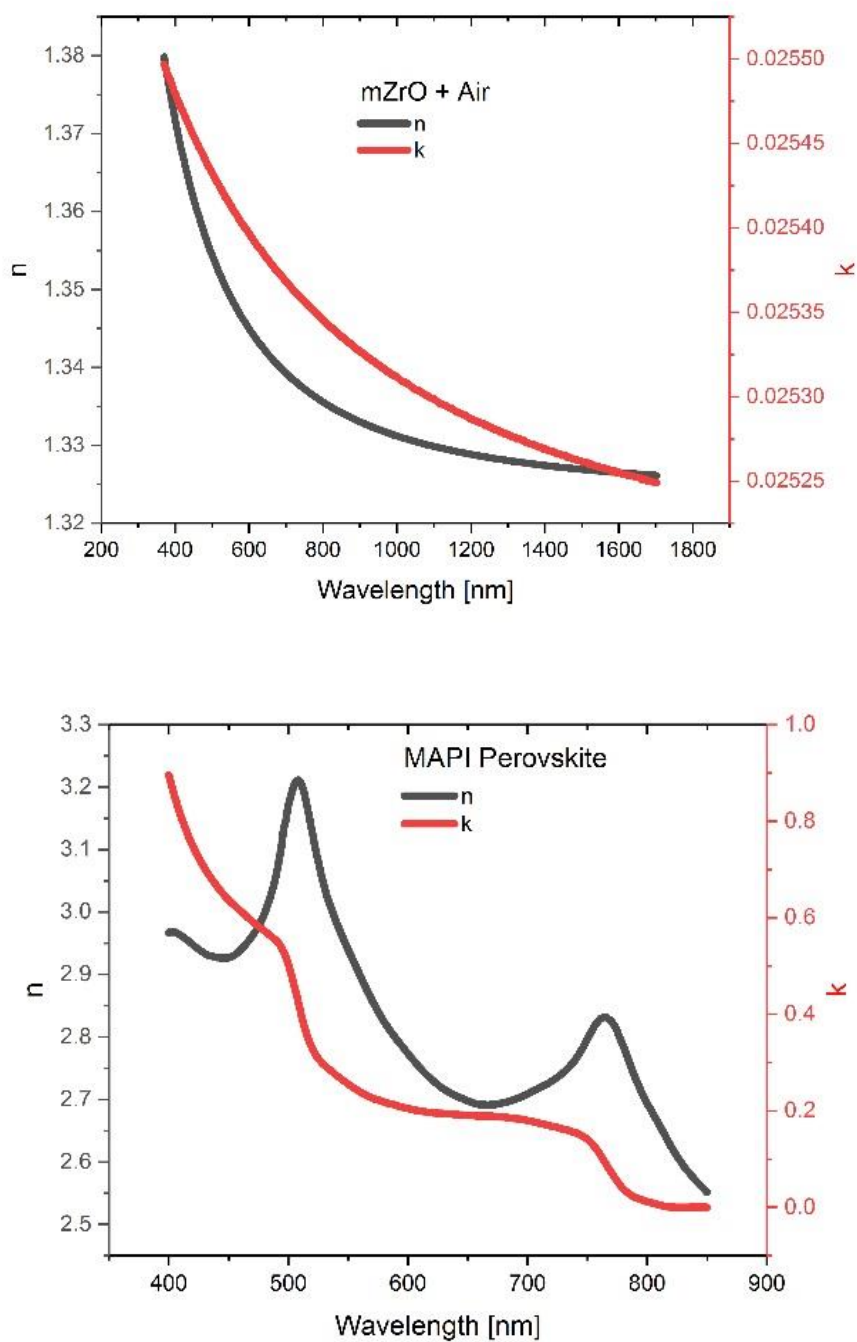


Figure S1. Optical Constants used in our Transfer Matrix modelling - from top to bottom: compact TiO₂, mesoporous Titania + air (51% porosity, Bruggeman model), mesoporous Zirconia + air (49% porosity, Bruggeman model, k is assumed 0 in the derivation of the final active layer constants, since this is likely a scattering relic), and MAPI perovskite as previously reported²⁷.

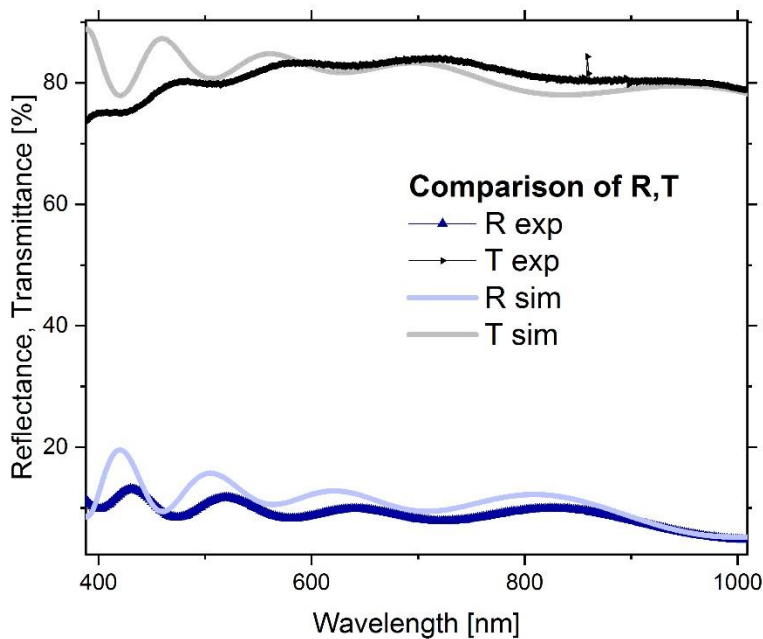
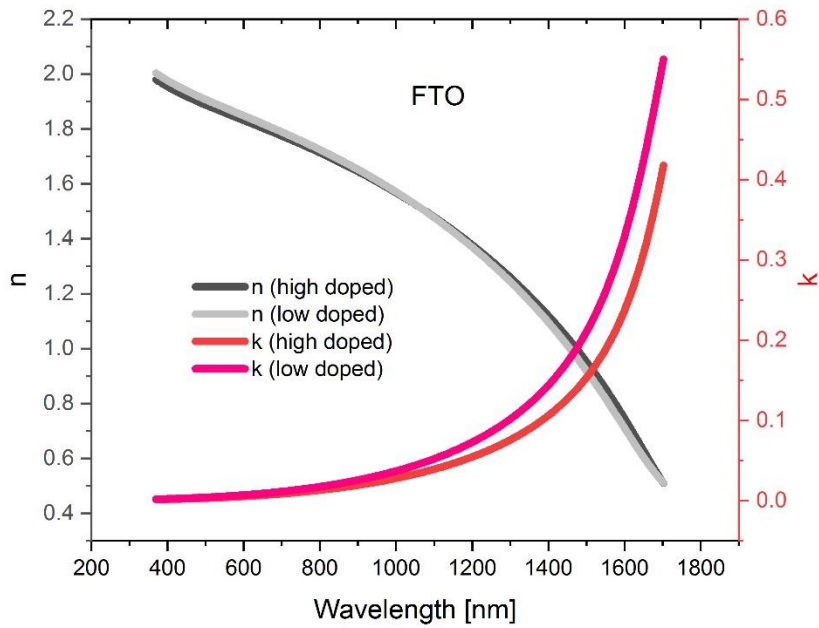


Figure S2. (Top) Optical constants of Fluorine-doped SnO (FTO). A good ellipsometry fit was found using subsequent layers of high-doped and low-doped FTO on a layer of undoped SnO. (Bottom) experimental Reflectance and Transmittance data of an FTO substrate compared with simulations using the Transfer Matrix approach and determined optical constants. Model interference peaks are more pronounced (higher visibility) towards the high-energy wavelengths, most likely due to scattering effects and glass absorption, not accounted for in the model but simulation and experiment are in good agreement with respect to fringe position.

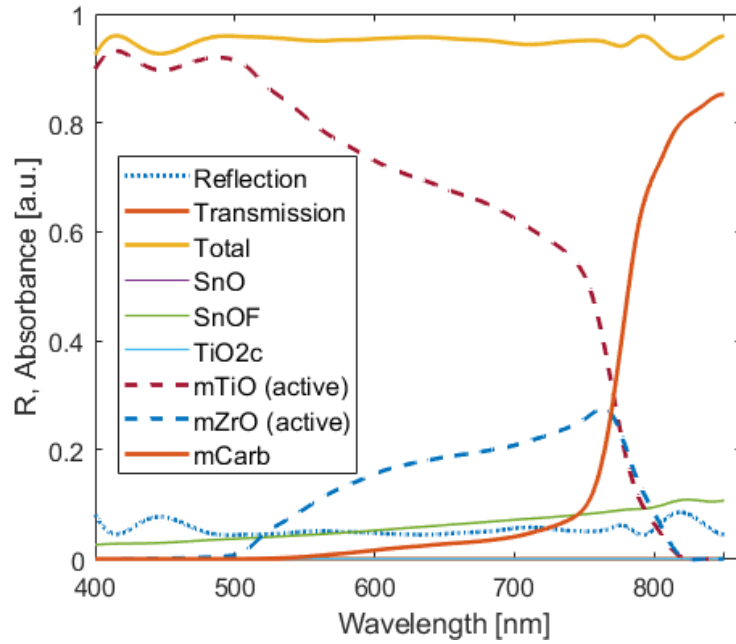


Figure S3. Layer absorptions calculated using our optical model. Note how m-Carbon (both the carbon conductor and perovskite within it) starts to absorb significantly around 760nm, which is probably indicative of the reason for the precipitous EQE model/device divergence beyond this wavelength.

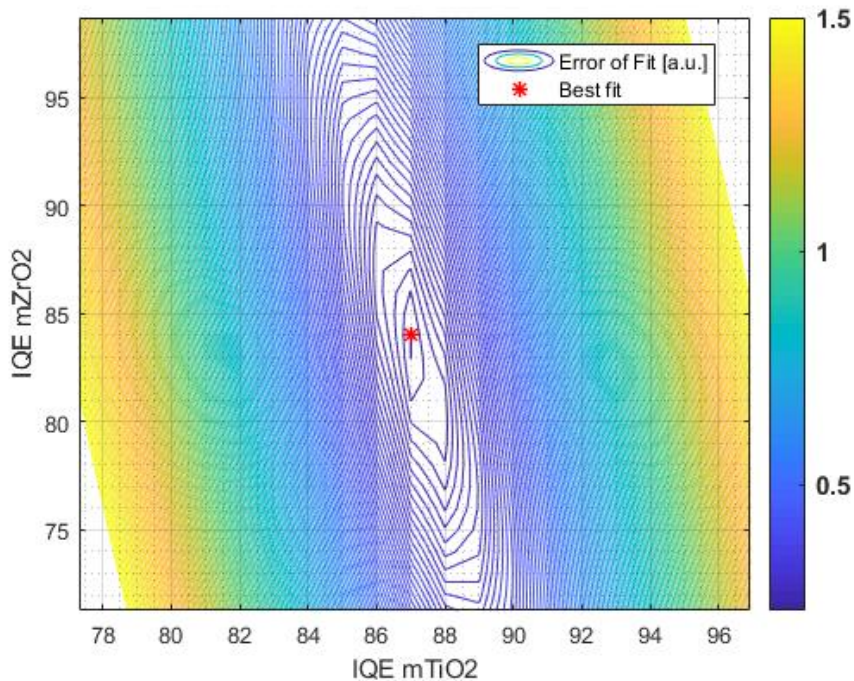


Figure S4. Sensitivity analysis of the IQE fitting, where the error is calculated as the norm of the difference between the simulated and experimental EQE. Sensitivity within a 4x4% grid is found to be 80 for the titania IQE and 10 for the zirconia IQE.